Letter

Tunable generation and propagation of vortex beams in a photonic chip

Jonathas M. de Oliveira,[1,3] Laura M. S. Santos,[2] Alcenisio J. Jesus-Silva,[2] and Eduardo J. S. Fonseca[2,*]

[1]*Federal Institute of Alagoas, Coruripe, Alagoas 57230-000, Brazil*

[2]*Institute of Physics, Federal University of Alagoas, Maceió, Alagoas 57072-900, Brazil*

[3]*Materials Graduate Program, Center of Technology, Federal University of Alagoas, Maceió, Alagoas 57072-900, Brazil*

(Received 26 April 2021; accepted 6 December 2021; published 20 December 2021)

We used a direct laser writing technique to build annular waveguides inside a glassy blade. These waveguides have shown the capability of generating orbital angular momentum beams with different topological charges in the same structure. Here we demonstrate that, after choosing suitable waveguide parameters, one may tune the topological charge of a beam just by tilting the input wavefront. This work opens opportunities for optical communications using spatial degrees of freedom multiplexed beams and for generation of tunable angular momentum at the microscale for integrability of lab on chips.

DOI: 10.1103/PhysRevA.104.L061501

I. INTRODUCTION

Optical vortex beams possess orbital angular momentum (OAM) connected to the phase of the field and to its intensity distribution [1]. Optical trapping, microfabrication, and communication systems are some of the potential applications associated with studies on vortex beams [2–6]. Beyond the singular beam's fundamentals and new applications there is a race to incorporate such optical fields and their many intrinsic degrees of freedom within the photonic devices. Compact and integrated optical elements need to be able to generate, transmit, process, and recover the information encoded by those structured beams.

Although the generation of these singular beams has been demonstrated by means of different methods, such as computer-generated holograms, metamaterials, photonic crystals, spiral phase plates, and diffractive optical elements [7–12], there is still the need to develop techniques and devices able to process helical beams into photonic chips composed of waveguides, directional couplers, beam splitters, and phase modulators.

Some works have demonstrated that fibers [13–18] and annular waveguides [19] can transmit light possessing OAM. Recently, it was demonstrated that light with OAM can be generated in waveguides embedded in a photonic chip [20]. The authors explained the OAM generation through a coupled wave theory where the light in a single mode waveguide evanescently couples to a waveguide supporting OAM. The coupling occurs when there is a match between the propagation constants of the two waveguides. Besides that, as demonstrated by Chen *et al.* [19,20], a "donut" shaped waveguide presents suitable geometry and physics conditions to guide and generate OAM beams. However, to guide a different topological charge it is necessary to change the waveguide structure to one with appropriate diameter.

In this Letter, we present the generation and guiding of optical beams carrying OAM with tunable topological charge. The topological charge of the output OAM beam basically depends on the phase of the input coupling beam. This means that just by properly tilting the input beam we can obtain different output OAM beams using the same waveguide structure, opening news possibilities to design photonics chips applied to different fields, such as optical communications, information processing, and integrated microfluidics.

II. EXPERIMENTAL SETUP

The direct laser writing technique [21] was used to build concentric cylindrical waveguides, with a "donut" transverse profile, inside boroaluminosilicate glassy blades (see Supplemental Material, Sec. A) [22]. A femtosecond laser has enough energy to start a nonlinear process in the material—multiphoton absorption, for instance—and subtly modify the refractive index only within the limit of the laser spot [23]. Figure 1(a) shows longitudinal (or frontal) phase contrast microscopy images of a 40 μm external diameter cylindrical transverse profile, and a 3 μm external diameter Gaussian waveguide in the center of the structure (see Supplemental Material, Sec. A) [22]. To analyze the refractive index change along the waveguide diameter we used the defocusing microscopy technique [24,25], with the same measurement scheme as in Fig. S1(b) but with transverse waveguide illumination. This technique consists of measuring the contrast C in two different defocus positions, one above and another below the zero-contrast position for each written line, thus obtaining the contrast difference ΔC of these two positions of opposite contrast [24]. This contrast difference is proportional to the change in the refractive index, as indicated by Fig. 1(b).

It is very important to realize that there are three different regions inside the annular structure which are adequate to guide the light, as shown in Fig. 1(c). During the femtosecond laser modification process, the refractive index changes

*eduardo@fis.ufal.br

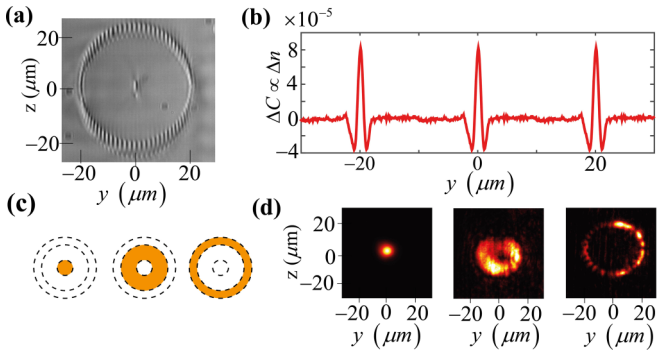

FIG. 1. Annular waveguide structure. (a) Microscopy image of cylindrical waveguide transverse profile. (b) Refractive index change of single line cross sections, modified by the femtosecond laser along the "donut" diameter. (c) Possible regions to guide the light inside the annular structure. (d) Output intensity profiles of the guided beams.

positively in the center of the laser spot but slightly negatively around the central region, as evidenced by Fig. 1(b) [25,26]. Therefore, it is perfectly possible to assume that different modes, including OAM modes, can propagate in the regions indicated in Fig. 1(b).

III. RESULTS AND DISCUSSION

Indeed, by directly coupling $m = 0$, $m = 1$, and $m = 2$ topological charges in the 40 μm diameter annular waveguide, we can observe in Fig. 1(d) the output intensity profiles for each one of these respective input beams (see Supplemental Material, Sec. B, for coupling methods) [22]. These results agree with Fig. 1(c), where each mode couples in a different region of the annular structure.

Additionally, it is important to point out that it is also possible to obtain different OAM modes even by coupling a Gaussian beam at the input port of the chip. Once the Gaussian beam is coupled, perfectly aligned to the waveguide axis, as shown in Fig. 2(a), we can tune to other topological charges by carefully varying the z transverse position of the waveguide related to the coupling axis ($z = 0$) using a yz stage. Figure 2(b) shows the well-known intensity profile of OAM beams and its corresponding far-field diffraction pattern by a triangular aperture [27,28]. Each topological charge was obtained for different z positions (vertical direction) or, equivalently, y positions (lateral direction). Such results are symmetric around the coupling reference axis. In fact, topological charges with opposite signals are located in opposite z (or y) positions around the reference axis, $z = y = 0$.

The propagation loss coefficient α [29], measured for different waveguides length, is about 0.3 dB/cm as expected for boroaluminosilicate glass [30]. However, the coupling efficiency decreases with higher-order OAM guided modes. The total optical loss, including coupling, propagation, and scattering on the waveguide walls, is estimated in Fig. 2(c) for each one of the guided modes.

The results presented here can be explained by a careful analysis of the wavefront that arrives at the annular

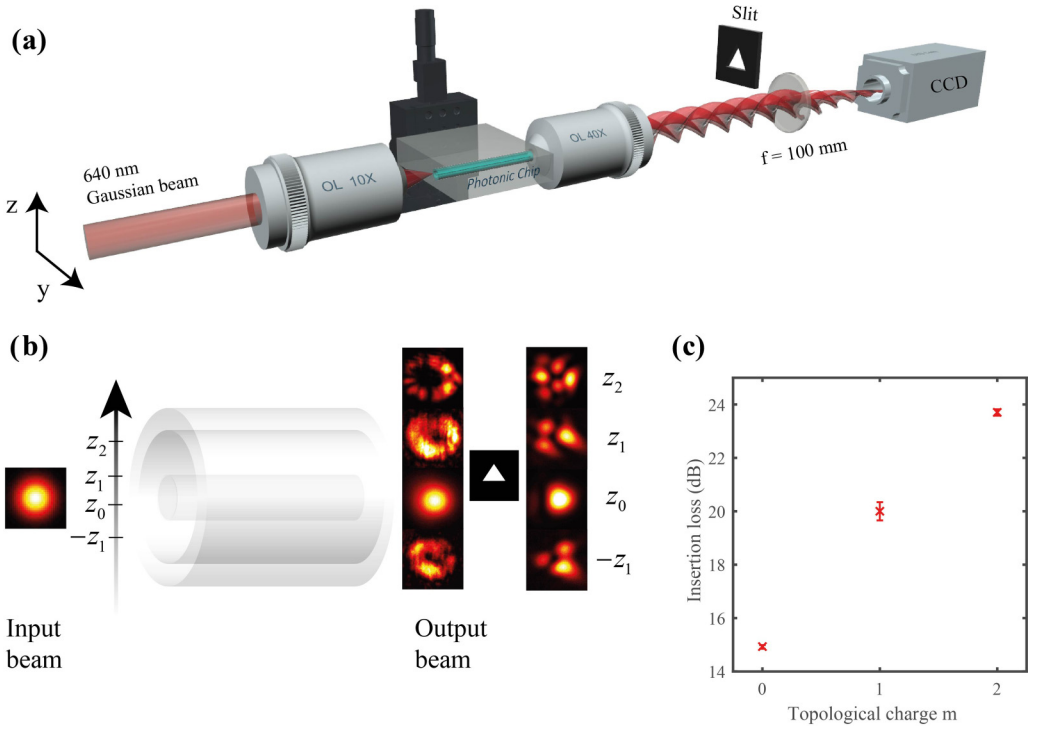

FIG. 2. Coupling an input Gaussian beam and tuning an output OAM beam. (a) Experimental setup to waveguide coupling and generation of OAM modes. (b) OAM modes in the waveguide output obtained by varying the z-position offset coupling. (c) Total optical loss of each propagating mode for 40 μm external diameter and 27 mm length waveguide. The error bars are the standard deviation of the measured insertion losses, considering P_{in} and P_{out} of three different waveguides with the same diameter and length.

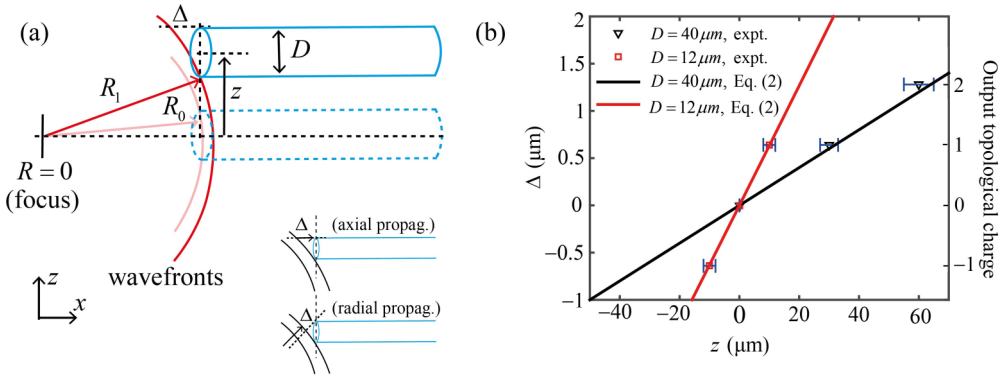

FIG. 3. Analysis of the wavefront coupling in the annular waveguide. (a) Spherical wavefront arriving at the annular waveguide. Inset: Path difference Δ considering axial or radial propagation of the wavefront. (b) Experimental points and the theoretical prediction given by Eq. (2) for the path difference Δ. The error bars are associated to the uncertainty in the measurement of the distance z.

waveguide. Figure 3(a) reveals that a transverse displacement z in relation to the coupling reference axis ($z = 0$) is related to an optical path difference Δ between these two points.

This same condition remains valid for any transverse displacement around the waveguide longitudinal x axis. For reasons of simplicity, we will consider only z-axis transverse displacements to analyze the generated phase difference.

Using a geometric optics approach, we can calculate the maximum path difference Δ associated to the z transverse position. We need to consider two possible configurations for the wavefront propagation in relation to the waveguide input [Fig. 3(a), inset], depending on the R distance to the focal plane: radial propagation for waveguides positioned very close to the objective lens focus, and axial propagation (along the x axis) for waveguides positioned far from the focal plane.

Assuming R_0 as the wavefront radius measured from the focal plane ($R = 0$) and D as the waveguide diameter, one may write the maximum path difference as

$$\Delta = \left[R_0^2 + \left(z + \frac{D}{2}\right)^2\right]^{1/2} - \left[R_0^2 + \left(z - \frac{D}{2}\right)^2\right]^{1/2}, \quad (1)$$

and

$$\Delta = R_0 - \sqrt{R_0^2 - 2Dz}, \quad (2)$$

where Eq. (1) represents the maximum optical path difference Δ, considering the radial propagation, and Eq. (2) considers the axial propagation (see Supplemental Material, Sec. B) [22]. It is important to point out that, for the experimental parameters used here, Eq. (1) has been reduced to Eq. (2).

Figure 3(b) shows excellent agreement between the experimental points and the theoretical prediction given by Eq. (2), for the z positions where the OAM beams should be generated. The experimental points were obtained using the experimental setup of Fig. 2(a) for two different waveguides ($D = 12\,\mu$m and $D = 40\,\mu$m), varying the z position until we have observed the OAM modes at the waveguide output. The theoretical points (continuous lines) were obtained by the substitution of the used values $R_0 = 190\,\mu$m ($R_0 = 2000\,\mu$m) with the waveguide of external diameter $D = 12\ \mu$m ($D = 40\,\mu$m) in Eq. (2). Interestingly enough, for a specific position z in Fig. 3(b), for instance, to $z = 10\,\mu$m, we have $\Delta = 0.63\,\mu$m (red line), which is approximately $\Delta \approx m\lambda$ where m represents the topological charge (an integer number) and λ is the wavelength. By a close inspection of the OAM beams in Fig. 2(b), it is possible to identify the topological charges m in graphs of Fig. 3(b) as illustrated by the triangles and squares. This leads us to understand that larger values of Δ are required to generate higher-order OAM modes.

As expected from Eqs. (1) and (2), there is a symmetry around the reference axis. We could observe the generation of opposite OAM modes when coupling the "donut" waveguide in opposite z positions (or y positions). As we can see in Fig. 2(b), the opposite OAM modes $m = +1$ and $m = -1$ are associated with symmetric z positions.

Although Eqs. (1) and (2) are simple expressions they seem very consistent in predicting different coupling positions of the waveguide in which an OAM beam can be generated inside the annular structure. In order to further verify this, we varied the R_0 longitudinal distance and z transverse distance, for a waveguide of $D = 40\,\mu$m external diameter, and localized the different positions in which $m = +1$ OAM beams were obtained. Figure 4(a) confirms the consistency and reliability between the experimental points and theoretical prediction, considering $\Delta \approx m\lambda$ (with $m = 1$).

So far, we have been disregarding a possible phase distortion on the wavefront of the input beam. We started to investigate how an intrinsic beam phase structure could contribute with the modes that would couple with the waveguide. In this case, we took as reference ($z = 0$) the same reference used when coupling a Gaussian beam, without an azimuthal phase structure. Maintaining all the geometric parameters ($D = 40\,\mu$m, $R_0 = 500\,\mu$m) fixed, the output modes depend on the azimuthal phase shift, owing to the Laguerre-Gauss beam with topological charge, leading to a different transversal displacement z for the corresponding output topological charge of a Gaussian input. Now we need to properly choose a new phase shift of the input beam and the transverse offset in order to tune a certain OAM beam in the waveguide output. This fact is clearly shown in Fig. 4(b).

Therefore, there is an adequate phase match Δ_{coupling} that allows the coupling of beams with a photonic chip in such

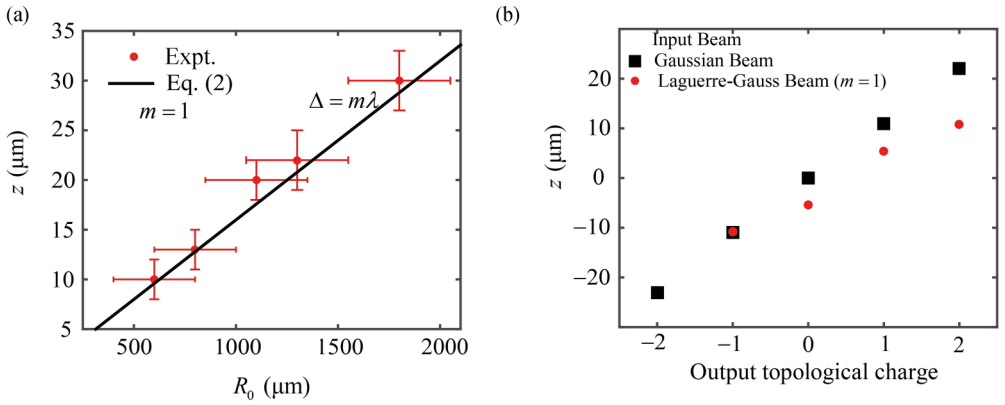

FIG. 4. Matching the input beam phase shift to the coupling parameters. (a) Geometrical parameters for coupling a $m = +1$ OAM beam. Experimental (red dots) and theoretical (black continuous line) points matching the coupling of the OAM, relating z and R_0 positions. All points agree with the relation $\Delta \approx m\lambda$. The error bars are associated to the uncertainty in the measurement of the distances z and R_0. (b) Output topological charge as a function of the transversal z position to Gaussian and Laguerre-Gauss input beams.

way that the input coupling phase depends on the coupling geometric parameters and on the phase shift of the input beam:

$$\Delta_{\text{coupling}} = \Delta(R_0, z, D) + \Delta_{\text{beam}}, \tag{3}$$

where $\Delta(R_0, z, D)$ is the phase difference generated by the coupling spatial parameters and Δ_{beam} corresponds to the optical path difference imposed to the wavefront during the coupling in each point of the "donut" waveguide input face.

For better characterization of the waveguide mode tunability we calculated some output modes' power spectra, all for a Gaussian input mode. In order to perform this task we first evaluated the output modes' phase, applying the Fourier transform method of fringe pattern analysis [31]. For each z position indicated on the top of each image in Fig. 5, the measured off-axis fringe patterns of the interference between the modes and a uniform plane wave is shown in the inset. After obtaining the complex field, we calculated the OAM components performing a transformation that linearly sorts all modes, assuming that the phase of each component mode is azimuthally symmetric and the amplitudes are radially symmetric (see Supplemental Material, Sec. C) [22]. The dominating modes in the power spectrum are indicated for each z position. In particular, $z = -11\,\mu$m, $z = 0\,\mu$m, $z = +11\,\mu$m, and $z = +20\,\mu$m, that correspond to OAM modes shown in Fig. 2(b), draw attention to the high purity of those modes, presenting normalized power at least 50% higher than other propagating and nonvisible modes [32]. When there are two dominating modes (for instance, $z = -16\,\mu$m, $z = -8\,\mu$m, $z = +7\,\mu$m, and $z = +15\,\mu$m), it is possible to note that these modes are spatially separated with negligible overlap. Such fact arises as a consequence of the propagation in different spatial regions of the waveguide [Fig. 1(b)].

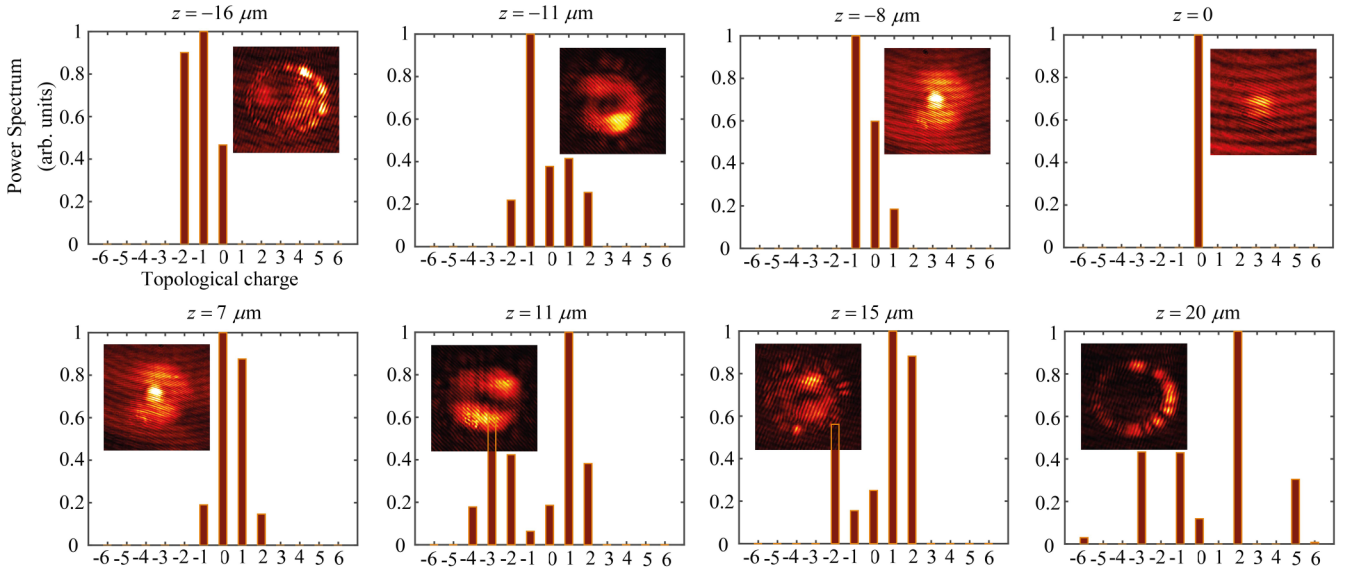

FIG. 5. Power spectra of the different output modes. The insets show the interference between the output modes and a reference plane wave. For each spectrum the dominating modes are indicated and related to the measured intensity. For example, in $z = 15\,\mu$m we can clearly see the modes of topological charge $m = 1$ and $m = 2$ in the inset, but in $z = 20\,\mu$m we just see the mode corresponding to $m = 2$.

IV. CONCLUSION

In summary, we show that the coupling between an OAM beam and a waveguide is described just by a phase shift and the output modes show reasonable purity, it even being possible to propagate two nonoverlapping, different modes at the same time. Our discoveries open a wide window of opportunities to the development of waveguides and photonic chips capable of generating and guiding different OAM modes in a simple way. The coupling basically depends on a single parameter Δ_{beam}, simplifying the design and waveguide writing process. These results can be useful for coupling of superpositions of OAM in waveguide structures for optical communications and information processing applications. Moreover, integrated microfluidic and photonic chips can benefit the possibility of guiding different OAM beam modes, useful for selecting different microparticle sizes in an embedded optical tweezer system.

ACKNOWLEDGMENTS

The present research was supported by Instituto Nacional de Ciência e Tecnologia de Informação Quântica [CNPq INCT-IQ (Grant No. 465469/2014-0)], Fundação de Amparo à Pesquisa do estado de Alagoas (FAPEAL), Conselho Nacional de Desenvolvimento Científico e Tecnológico (CNPq), and Coordenação de Aperfeiçoamento de pessoal de Nível Superior, Finance Code No. 001 (CAPES).

[1] H. Rubinsztein-Dunlop, A. Forbes, M. Berry, M. Dennis, D. Andrews, M. Mansuripur, C. Denz, C. Alpmann, P. Banzer, T. Bauer *et al.*, J. Opt. **19**, 013001 (2016).

[2] C. Rosales-Guzmán, B. Ndagano, and A. Forbes, J. Opt. **20**, 123001 (2018).

[3] M. Chen, S. Huang, X. Liu, Y. Chen, and W. Shao, Appl. Phys. B **125**, 184 (2019).

[4] L. Yang, D. Qian, C. Xin, Z. Hu, S. Ji, D. Wu, Y. Hu, J. Li, W. Huang, and J. Chu, Appl. Phys. Lett. **110**, 221103 (2017).

[5] A. Ablez, K. Toyoda, K. Miyamoto, and T. Omatsu, OSA Continuum **4**, 403 (2021).

[6] B. Ndagano, I. Nape, M. A. Cox, C. Rosales-Guzman, and A. Forbes, J. Lightwave Technol. **36**, 292 (2018).

[7] Y. Shen, X. Wang, Z. Xie, C. Min, X. Fu, Q. Liu, M. Gong, and X. Yuan, Light: Sci. Appl. **8**, 90 (2019).

[8] P. Li, Y. Zhang, S. Liu, C. Ma, L. Han, H. Cheng, and J. Zhao, Opt. Lett. **41**, 2205 (2016).

[9] D. Zhang, X. Cao, H. Yang, J. Gao, and X. Zhu, Opt. Express **26**, 24804 (2018).

[10] K. Zhang, Y. Wang, Y. Yuan, and S. N. Burokur, Appl. Sci. **10**, 1015 (2020).

[11] B. Wang, W. Liu, M. Zhao, J. Wang, Y. Zhang, A. Chen, F. Guan, X. Liu, L. Shi, and J. Zi, Nat. Photonics **14**, 623 (2020).

[12] J. M. Oliveira, A. J. Jesus-Silva, and E. J. S. Fonseca, Opt. Laser Technol. **119**, 105632 (2019).

[13] A. Wang, L. Zhu, L. Wang, J. Ai, S. Chen, and J. Wang, Opt. Express **26**, 10038 (2018).

[14] S. Li, Q. Mo, X. Hu, C. Du, and J. Wang, Opt. Lett. **40**, 4376 (2015).

[15] B. M. Heffernan, R. D. Niederriter, M. E. Siemens, and J. T. Gopinath, Opt. Lett. **42**, 2683 (2017).

[16] J. A. Borda-Hernández, C. M. Serpa-Imbett, and H. E. H. Figueroa, Polymers **12**, 2776 (2020).

[17] S. Ramachandran and P. Kristensen, Nanophotonics **2**, 455 (2013).

[18] N. Bozinovic, Y. Yue, Y. Ren, M. Tur, P. Kristensen, H. Huang, A. E. Willner, and S. Ramachandran, Science **340**, 1545 (2013).

[19] Y. Chen, J. Gao, Z.-Q. Jiao, K. Sun, W.-G. Shen, L.-F. Qiao, H. Tang, X.-F. Lin, and X.-M. Jin, Phys. Rev. Lett. **121**, 233602 (2018).

[20] Y. Chen, K.-Y. Xia, W.-G. Shen, J. Gao, Z.-Q. Yan, Z.-Q. Jiao, J.-P. Dou, H. Tang, Y.-Q. Lu, and X.-M. Jin, Phys. Rev. Lett. **124**, 153601 (2020).

[21] J. M. Oliveira, A. J. Jesus-Silva, A. C. A. Silva, N. O. Dantas, and E. J. S. Fonseca, Opt. Mater. **101**, 109767 (2020).

[22] See Supplemental Material at http://link.aps.org/supplemental/10.1103/PhysRevA.104.L061501 for annular waveguide writing process, imaging and coupling methods, and power spectra measurement.

[23] R. Osellame, G. Cerullo, and R. Ramponi, *Femtosecond Laser Micromachining: Photonic and Microfluidic Devices in Transparent Materials* (Springer, Berlin, 2012).

[24] E. Lages, W. Cardoso, G. F. B. Almeida, L. Siman, O. Mesquita, C. R. Mendonça, U. Agero, and S. Pádua, Appl. Opt. **57**, 8699 (2018).

[25] T. T. Fernandez, S. Gross, A. Arriola, K. Privat, and M. J. Withford, Opt. Express **28**, 10153 (2020).

[26] A. Arriola, S. Gross, N. Jovanovic, N. Charles, P. G. Tuthill, S. M. Olaizola, A. Fuerbach, and M. J. Withford, Opt. Express **21**, 2978 (2013).

[27] J. M. Hickmann, E. J. S. Fonseca, W. C. Soares, and S. Chávez-Cerda, Phys. Rev. Lett. **105**, 053904 (2010).

[28] W. Soares, A. Moura, A. Canabarro, E. de Lima, J. Lopes, E. Fonseca, M. Felisberto, B. de Lima Bernardo, J. Hickmann, and S. Chávez-Cerda, Appl. Opt. **59**, 5687 (2020).

[29] R. G. Hunsperger, *Integrated Optics: Theory and Technology* (Springer, New York, 2009).

[30] I. Pitsios, F. Samara, G. Corrielli, A. Crespi, and R. Osellame, Sci. Rep. **7**, 11342 (2017).

[31] M. Takeda, H. Ina, and S. Kobayashi, J. Opt. Soc. Am. **72**, 156 (1982).

[32] J. Xu, L. Chen, X. Zhai, R. Zhang, K. D. Mcdonald-Maier, S. Huang, and K. Bi, Eng. Sci. **10**, 51 (2020).